

A LIDAR FOR REMOTE SENSING OF OPTICAL TURBULENCE

**W. R. Dagle, M. S. Belen'kii, G. G. Gimmestad, D. W. Roberts,
and J. M. Stewart**

**Applied Technologies, Inc.
1120 Delaware Ave.
Longmont, CO 80501**

April 2000

Final Report

APPROVED FOR PUBLIC RELEASE; DISTRIBUTION IS UNLIMITED.

20000620 048



**AIR FORCE RESEARCH LABORATORY
Directed Energy Directorate
3550 Aberdeen Ave SE
AIR FORCE MATERIEL COMMAND
KIRTLAND AIR FORCE BASE, NM 87117-5776**

Using Government drawings, specifications, or other data included in this document for any purpose other than Government procurement does not in any way obligate the U.S. Government. The fact that the Government formulated or supplied the drawings, specifications, or other data, does not license the holder or any other person or corporation; or convey any rights or permission to manufacture, use, or sell any patented invention that may relate to them.

This report has been reviewed by the Public Affairs Office and is releasable to the National Technical Information Service (NTIS). At NTIS, it will be available to the general public, including foreign nationals.

If you change your address, wish to be removed from this mailing list, or your organization no longer employs the addressee, please notify AFRL/DEBA, 3550 Aberdeen Ave SE, Kirtland AFB, NM 87117-5776.

Do not return copies of this report unless contractual obligations or notice on a specific document requires its return.

This report has been approved for publication.



FRANK D. EATON
Project Manager



KIMBERLEY A. McCRAE
Chief, Airborne Laser Technology Branch

FOR THE COMMANDER



R. EARL GOOD, SES
Director, Directed Energy

REPORT DOCUMENTATION PAGE

Form Approved
OMB No. 0704-0188

Public reporting burden for this collection of information is estimated to average 1 hour per response, including the time for reviewing instructions, searching existing data sources, gathering and maintaining the data needed, and completing and reviewing this collection of information. Send comments regarding this burden estimate or any other aspect of this collection of information, including suggestions for reducing this burden to Department of Defense, Washington Headquarters Services, Directorate for Information Operations and Reports (0704-0188), 1215 Jefferson Davis Highway, Suite 1204, Arlington, VA 22202-4302. Respondents should be aware that notwithstanding any other provision of law, no person shall be subject to any penalty for failing to comply with a collection of information if it does not display a currently valid OMB control number. PLEASE DO NOT RETURN YOUR FORM TO THE ABOVE ADDRESS.

1. REPORT DATE (DD-MM-YYYY) 01-04-2000	2. REPORT TYPE Final	3. DATES COVERED (From - To) 30 Apr 1999 to 29 Mar 2000		
4. TITLE AND SUBTITLE A Lidar for Remote Sensing of Optical Turbulence		5a. CONTRACT NUMBER F29601-99-C-0060		
		5b. GRANT NUMBER		
		5c. PROGRAM ELEMENT NUMBER 65502F		
6. AUTHOR(S) Dagle, W. R., Belen'kii, Mikhail S.,* Gimmestad, G. G.,* Roberts, D. W.,* Stewart, J. M.*		5d. PROJECT NUMBER 3005		
		5e. TASK NUMBER DO		
		5f. WORK UNIT NUMBER CA		
7. PERFORMING ORGANIZATION NAME(S) AND ADDRESS(ES) Applied Technologies, Inc. 1120 Delaware Ave. Longmont, CO 80501		8. PERFORMING ORGANIZATION REPORT NUMBER 8718		
9. SPONSORING / MONITORING AGENCY NAME(S) AND ADDRESS(ES) AFRL/DEBA Dr. Frank D. Eaton 3550 Aberdeen Ave. SE Kirtland AFB, NM 87117-5776		10. SPONSOR/MONITOR'S ACRONYM(S) 11. SPONSOR/MONITOR'S REPORT NUMBER(S) AFRL-DE-TR-2000-1022		
12. DISTRIBUTION / AVAILABILITY STATEMENT Approved for Public Release; Distribution is Unlimited.				
13. SUPPLEMENTARY NOTES *Georgia Institute of Technology Atlanta, GA 30332-0834				
14. ABSTRACT Atmospheric turbulence affects the performance of missile defense platforms, such as the Airborne Laser (ABL). To understand the results of laser propagation tests on both the horizontal and inclined propagation paths, and to validate atmospheric turbulence prediction models, the vertical profile of the refractive index structure parameter is required. There is no current accepted lidar method for measuring profiles of the refractive index structure parameter. The differential image motion (DIM) has been established as the best way to measure the Fried parameter for "seeing" using a star or laser source. A new concept was proposed, DIM lidar, for measuring vertical profiles of the refractive index structure parameter. The lidar has the transmitter and receiver at the same end of the optical path and uses a pulsed lidar, atmospheric backscatter, and a range-gated receiver. A proof-of-concept test was performed and the experimental results validated the DIM lidar concept and showed that the refractive index structure parameter can be accurately measured.				
15. SUBJECT TERMS Lidar, laser, differential image motion, refractive index structure parameter, optical turbulence, ABL,				
16. SECURITY CLASSIFICATION OF: a. REPORT Unclassified		17. LIMITATION OF ABSTRACT Unlimited	18. NUMBER OF PAGES 36	19a. NAME OF RESPONSIBLE PERSON Dr. Frank D. Eaton
b. ABSTRACT Unclassified		19b. TELEPHONE NUMBER (include area code) 505-853-1091		
c. THIS PAGE Unclassified				

This page left intentionally blank

TABLE OF CONTENTS

SF298.....	i
Blank Page	ii
Table of Contents	iii
List of Figures.....	iv
List of Tables	v
Blank Page	vi
1.0 INTRODUCTION.....	1
2.0 PHASE I TECHNICAL OBJECTIVES AND MILESTONES.....	2
3.0 ACCOMPLISHMENTS	2
3.1 CONCEPTUAL DESIGN	3
3.1.1 <i>DIM lidar concept</i>	3
3.1.2 <i>Theoretical underpinnings of the DIM lidar</i>	4
3.1.3 <i>Effect of the outer scale of turbulence</i>	6
3.2 PERFORMANCE ANALYSIS.....	7
3.2.1 <i>3.2.1. Turbulent calculations</i>	7
3.2.2 <i>Lidar calculations</i>	14
3.3 HARDWARE AND SOFTWARE DEVELOPMENT.....	17
3.3.1 <i>3.3.1 Hardware development</i>	17
3.3.2 <i>Software development</i>	19
3.4 FIELD TEST.....	20
3.5 ANALYSIS OF THE DATA	21
3.6 SCIENTIFIC PAPER	24
3.7 EFFECTS OF LASER SPECKLES AND SCINTILLATIONS.....	24
3.7.1 <i>Laser speckle phenomenon</i>	24
3.7.2 <i>Coherent point source</i>	25
3.7.3 <i>Extended incoherent source</i>	26
3.7.4 <i>Error analysis</i>	29
3.7.5 <i>Laser scintillations</i>	30
3.7.6 <i>Sky background</i>	32
3.7.7 <i>Design consideration</i>	32
3.7.8 <i>Summary</i>	32
4.0 CONCLUSIONS.....	33

LIST OF FIGURES

Figure 1	Differential Image Motion Lidar	3
Figure 2	Effect of outer scale.....	7
Figure 3	Diagram of the hard-target analog of the DIM lidar used in the field test	18
Figure 4	Time histories of the values measured with a commercial scintillometer and the hard-target analog of the DIM lidar	22
Figure 5	Scatter plot of the measurements with the hard-target analog of the DIM lidar versus the scintillometer data.....	23
Figure 6	(a – c) Images collected with hard-target analog of the DIM lidar in very weak (a), moderate (b), and very strong turbulence condition (c)	28

LIST OF TABLES

Table 1	Proof-Of-Concept Test	10
Table 2	Airborne Laser Advanced Concepts Testbed	11
Table 3	Airborne Laser Advanced Concepts Testbed	11
Table 4	Airborne Laser Advanced Concepts Testbed	12
Table 5	Astronomy	12
Table 6	Airborne Laser Scenario	13
Table 7	Airborne Laser Scenario	13
Table 8	ABL-ACT – 50 km Range.....	16
Table 9	Astronomy	16
Table 10	ABL – 100 km Range	16
Table 11	ABL – 300 km Range	17

This page left intentionally blank

1.0 INTRODUCTION

Atmospheric turbulence affects the performance of missile defense platforms, such as the Airborne Laser (ABL). To understand the results of laser propagation tests on both horizontal and inclined propagation paths, and to validate atmospheric turbulence prediction models, the vertical profile of the refractive index structure characteristic $C_n^2(h)$ is required. The astronomical and adaptive optics communities have established

several optical techniques¹ for measuring path-integrated values of $\bar{C}_n^2 = \int_0^{\infty} C_n^2(h)dh$ or the

Fried parameter, r_0 , but these methods do not provide path-resolved information. In order to remotely sense a vertical profile of C_n^2 , a true lidar is required.

A number of lidar techniques for measuring $C_n^2(h)$ have been proposed. These methods were based on turbulent broadening of a laser beam,²⁻⁴ the residual turbulent scintillation effect,⁵ and laser beam motion.⁶ Measurements of atmospheric C_n^2 values with a bistatic CW lidar were reported in Ref. 3. However, despite these developments, there is currently no accepted lidar method for measuring profiles of $C_n^2(h)$.

The differential image motion (DIM) method has already been established in astronomy as the best way to measure the Fried parameter, r_0 , but all of the previous work used a star or a laser at one end of an optical path and a receiver at the other. For this reason, only path-integrated quantities such as r_0 can be measured with this method.

The Applied Technologies Inc. and Georgia Tech Research Institute team proposed a new concept, DIM lidar, for measuring vertical profiles of $C_n^2(h)$. A lidar has the transmitter and receiver at the same end of the optical path, and it uses a pulsed laser, atmospheric backscatter, and a range-gated receiver to probe the atmosphere at various ranges. Phase I of the SBIR was an investigation of this concept.

2.0 PHASE I TECHNICAL OBJECTIVES AND MILESTONES

The overall objective of Phase I was to demonstrate the technical feasibility of the DIM lidar concept by developing and testing a hard-target analog of this lidar.

The Phase I work plan included six tasks:

- Conceptual design;
- Performance analysis;
- Hardware and software development;
- Field test;
- Data analysis; and
- Scientific paper and final report.

The work was planned for nine months. A mid-term review and a briefing were scheduled on September 2, 1999, and delivery of the final report was scheduled in February, 2000.

3.0 ACCOMPLISHMENTS

All planned tasks were accomplished. The results from Phase I were presented at a briefing at the sponsor facility on September 2, 1999. Hardcopies of the briefing materials were delivered to the Technical Monitor. Additional work, which includes the analysis of the effects of a speckle phenomenon and scintillation on the performance of the DIM lidar, was documented in a Technical Memorandum dated September 1999, which was also delivered. The accomplishments for each task are described in the following sections.

3.1 Conceptual Design

3.1.1 DIM lidar concept

The concept of the DIM lidar is illustrated in Fig.1. This lidar employs common transmit/receive optics and a range-gated focal plane array. The lidar operates as follows: pulsed laser beam is transmitted through a common transmit/receive aperture and is focused at the desired measurement distance. Scattered laser irradiance is received through two spatially separated sub-apertures. The motion of two images of the laser beam in the scattering volume is measured in the image plane. The statistics of the differential motion of the two images relates to the strength of optical turbulence along the path, which is characterized by the refractive index structure characteristic C_n^2 . By measuring the differential motion of a reflected laser spot over various distances, a profile of C_n^2 is estimated.

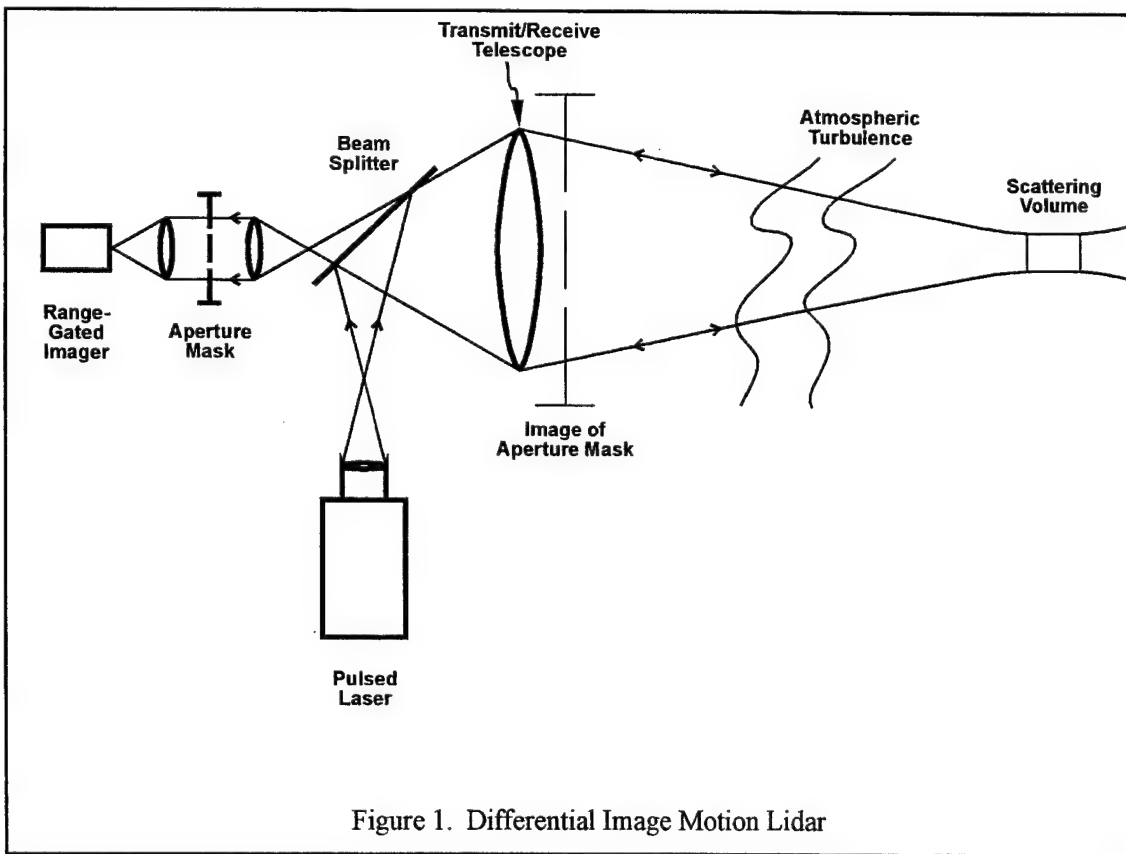


Figure 1. Differential Image Motion Lidar

3.1.2 Theoretical underpinnings of the DIM lidar

An analytical expression for the differential image motion variance is known for the conventional DIM technique.⁷ For the lidar configuration it was established under this task. In the lidar scheme, an optical wave propagates through the turbulent medium twice: from the lidar to the scattering volume, and back to the receiver. For a common transmit/receive configuration, the image displacements can be presented in the form

$$\varphi_1 = \varphi_B - \varphi_{1,R}, \quad (1)$$

$$\varphi_2 = \varphi_B - \varphi_{2,R}, \quad (2)$$

where φ_1 and φ_2 are the centroid positions of the two images, φ_B is the displacement due to the wavefront tilt of the transmitted beam, and $\varphi_{1,R}$ and $\varphi_{2,R}$ are the displacements due to the wavefront tilts of the reflected wave in the two receiving apertures. The minus signs in equations (1) and (2) take into account that the transmitted beam and the reflected wave propagate in opposite directions. By subtracting Eq. (1) from Eq. (2) one can show that the differential image motions on one-way and two-way propagation paths coincide with each other, i. e. $\varphi_d = \varphi_1 - \varphi_2 = \varphi_{2,R} - \varphi_{1,R}$, and so the differential image motion variance for a lidar is given by

$$\sigma_d^2 = \langle \varphi_d^2 \rangle = \langle (\varphi_{2,R} - \varphi_{1,R})^2 \rangle. \quad (3)$$

The implication is that one can use the same expression derived for the conventional one-way scheme⁷ for the lidar configuration. This expression has the form

$$\bar{C}_n^2 = \frac{(\sigma_d / f)^2 d^{1/3}}{11.6[1 - 0.694(d / \mu)^{1/3}]}, \quad (4)$$

where $\bar{C}_n^2 = \int_0^L C_n^2(x)(1 - x/L)^{5/3} dx$, L is the distance between the lidar and the scattering

volume, f is the focal length of the receiving telescope, d is the sub-aperture diameter, and μ is the separation between the sub-apertures. Eq.(4) takes into account the spherical divergence of the reflected wave. For a horizontal path where C_n^2 is constant, $\bar{C}_n^2 = (3/8)LC_n^2$. Eqs. (3) and (4) is also valid for a bistatic lidar configuration.

The absolute value of the image motion variance in each receiving channel of the DIM lidar for common transmit/receive optics is given by⁸

$$\langle \varphi_{1,2}^2 \rangle = 4.04(a_0^{-1/3} + d^{-1/3} - 2^{7/6}(a_0^2 + d^2)^{-1/6}) \int_0^L C_n^2(\xi)(1 - /L)^{5/3} d\xi, \quad (5)$$

where a_0 is the transmitting aperture diameter, and $a_0 > d$. For a bistatic configuration, where the wavefront tilt of the transmitted beam and the reflected wave are uncorrelated, this equation has the form

$$\langle \varphi_{1,2}^2 \rangle = 4.04(a_0^{-1/3} + d^{-1/3}) \int_0^L C_n^2(\xi)(1 - /L)^{5/3} d\xi. \quad (6)$$

According to Eq. (5), when the transmitter diameter is equal to the receiver diameter $a_0 \rightarrow d$, the centroid variance equals zero $\langle \varphi_{1,2}^2 \rangle \rightarrow 0$. This is caused by reciprocity, i.e. the fact that the transmitted beam and the reflected wave propagate through the same turbulent eddies. However, even for common transmit/receive optics the absolute variances $\langle \varphi_{1,2}^2 \rangle$ have a non-zero value when $a_0 > d$. Besides, from Eqs. (1)-(3) it is seen that since the differential image motion, φ_d , does not depend on the beam wander component, φ_B , so reciprocity does not affect the performance of the DIM lidar.

The DIM method has numerous advantages over other proposed techniques. Because it measures the differential motion of images and not their sizes, it is fundamentally

immune to any effects that cause image blurring, such as vibration, laser instability, diffraction on the transmitting and receiving apertures, environmental changes in the system MTF, and aerosol image blurring. It is not affected by reciprocity, and the DIM technique has been shown to be immune to variations of the outer scale of turbulence. This effect is considered in the next section. For all these reasons, the DIM technique is much more robust than methods based on laser beam broadening and beam motion.

In addition, the proposed lidar is based on direct detection (rather than coherent detection), which means that it can be built largely from commercial, off-the-shelf components, and the optical assembly will not have a requirement for extreme stability. The astronomical and adaptive optics communities have already established the technology base for the DIM lidar. Development of a prototype would be low-risk and cost-effective.

3.1.3 Effect of the outer scale of turbulence

An analysis of the effect of the outer scale of turbulence on the DIM technique is presented in this section. In an experiment performed at the Starfire Optical Range (SOR) at Kirtland Air Force Base¹ three optical methods including a) the DIM technique, b) the long-exposure PSF, and c) the short-exposure PSF methods were compared. The Fried parameter measured with these three sensors is shown in Fig. 2. The data from the DIM and long-exposure PSF sensors are marked as ATMOS and MTF, respectively, whereas the data from the short-exposure PSF sensor are marked as SHORT EXP.

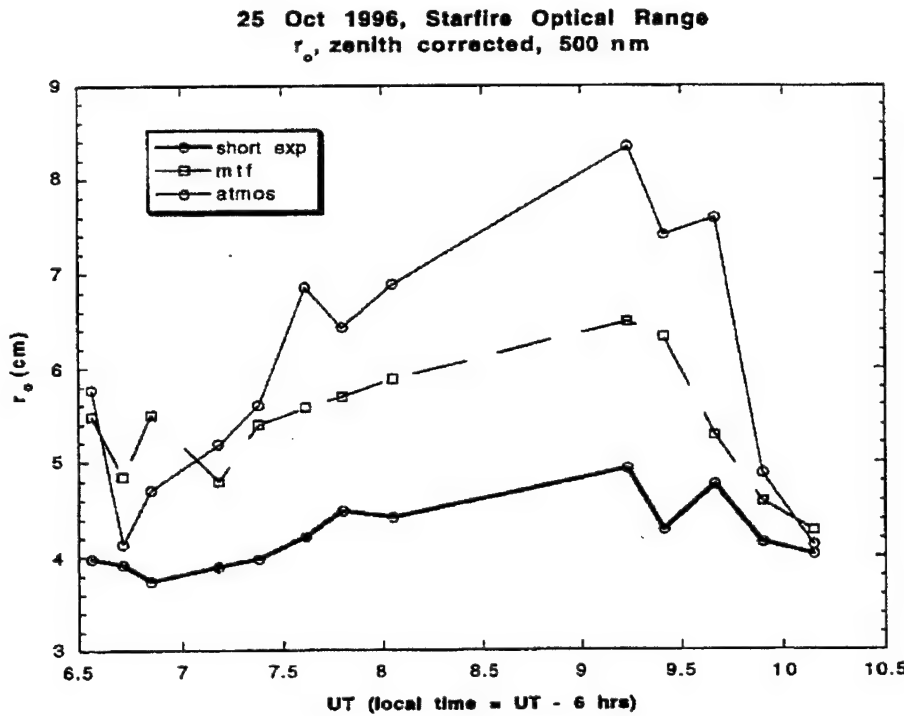


Figure 2. The Effect of Outer Scale

The comparison revealed that, for some conditions significant differences (up to a factor of 2) between the readings from the three sensors has been observed. An analysis performed by researchers at Georgia Tech showed that the three methods have different sensitivities to the variations of the outer scale of turbulence, L_0 , and the DIM method is the least sensitive to this effect. This is because large-scale wavefront aberrations caused by the outer scale of turbulence are cancelled in the differential motion. This analysis was performed by using the von Karmann power spectrum of turbulence, which includes a finite outer scale, L_0 .

3.2 Performance Analysis

3.2.1 3.2.1. Turbulent calculations

Under this task a performance analysis of the DIM lidar was performed, including quantitative characterization of the laser spot size in the image plane and the amount of

motion of this image spot. This analysis also includes characterization of the signal-to noise ratio, and the centroid error caused by a finite number of photons. Parameters of the laser beam and reflected spot in the image plane were estimated for four propagation scenarios: 1) a proof-of-concept test over 300 m, 2) tests at the ABL advanced Concept Test Bed (ACT), 3) profiling of C_n^2 at astronomical sites, and 4) measurements of C_n^2 aboard the ABL platform. Since the above scenarios include different measurement ranges, which vary from 300 m up to 300 km, different laser sources were considered for each case. A He-Ne 25 mW laser was considered for the proof-of-concept test over 300 m. A Q-switched, doubled Nd:YAG, operating at 532 nm and transmitting 10 W laser power was planned for the ABL ACT test. An eye-safe UV laser operating at 351nm was considered for the commercial astronomical application. Finally, a pulsed laser operating at 1.06 μ m with an energy 1 J per pulse and a pulse repetition rate of 1 kHz was planned for the ABL scenario.

The estimated parameters include the coherence radius, or Fried parameter, r_0 , long-exposure beam size, φ_{eff} , short-exposure beam size, φ_{ST} (which determines an instantaneous spot size in the image plane), beam wander standard deviation, σ_c , and rms differential motion, σ_d . The long-exposure angular size of the beam is given by the known formula⁹

$$\varphi_{eff}^2 = (a_{eff}/L)^2 = (a_0/L)^2(1 - L/F_i)^2 + (1/ka_0)^2 + (2/k\rho_c)^2, \quad (7)$$

where L is the distance, F_i is the initial radius of curvature of the beam, a_0 is the radius of the transmitting aperture, $k = 2\pi/\lambda$ is the wavenumber, and $\rho_c = (1.45k^2 \int_0^L C_n^2(z)(1 - z/L)^{5/3} dz)^{-3/5}$ is the coherence radius of a spherical wave. For $C_n^2 = const.$ this radius relates to the coherence radius of a plane wave, ρ_0 , by $\rho_c = 1.8\rho_0$ and to the Fried parameter, r_0 , by $r_0 = 1.1\rho_c$.

The short-exposure radius of the beam, a_{SE} , according to Ref. 10, relates to the long-exposure beam radius, a_{eff} , and rms beam wander, $\langle \varphi_B^2 \rangle^{1/2}$, by the equation

$$a_{eff}^2 = a_{SE}^2 + \langle \varphi_B^2 \rangle \quad (8)$$

Consequently, the short-exposure beam radius is $a_{SE} = (a_{eff}^2 - \langle \varphi_B^2 \rangle)^{1/2}$. The two-axis beam wander variance for a focused beam, has the form¹⁰

$$\langle \varphi_B^2 \rangle = 1.51 C_n^2 a_0^{-1/3} \quad (9)$$

Table 1 presents the estimated parameters of the transmitted beam and reflected laser spot in the image plane for the proof-of-concept test. The expected values of C_n^2 are from $10^{-14} m^{-2/3}$ to $5 \cdot 10^{-13} m^{-2/3}$, the transmitter diameter is $2a_0 = 0.09 m$, the sub-aperture diameter and the separation are $d = 0.11 m$ and $\mu = 0.11 m$, respectively. It is seen that the short-exposure beam size is in the range from $3.5 \mu rad$ to $39 \mu rad$, whereas rms differential motion is in the range from $2.9 \mu rad$ to $20 \mu rad$. Importantly, that rms differential motion is comparable to the short exposure size of the beam, and consequently, to the instantaneous spot size in the image plane. This suggests that the differential image motion can be accurately measured. The proof-of-concept test performed under task 4 confirmed this conclusion.

Tables 2, 3, and 4 present estimated parameters of the transmitted beam and reflected laser spot in the image plane for the ABL ACT scenario. The selected values of C_n^2 ($C_n^2 = 2 \cdot 10^{-17} m^{-2/3}$, $6 \cdot 10^{-17} m^{-2/3}$ and $2 \cdot 10^{-16} m^{-2/3}$), correspond to the values of the Fried parameter of $r_0 = 20 cm$, $10 cm$, and $4 cm$ measured at the wavelength of $1.06 \mu m$ on the $50 km$ propagation path. The absolute values of the estimated rms differential motion and short-exposure beam size in this case are smaller than that for the proof-of-concept test, but they are comparable to each other. Therefore, the image motion of a reflected

spot can be accurately measured for the ABL ACT test as well. The estimates given in Tables 2, 3, and 4 would be useful for the design of the DIM lidar for the ABL ACT test site.

Table 5 shows system parameter estimates for the astronomical scenario. An eye-safe UV laser was considered in this case. The path-integrated values of \bar{C}_n^2 , which correspond to values of the Fried parameter in the range from 5 cm to 20 cm, were selected. These values of r_0 correspond to a 500 nm wavelength and are corrected to the zenith.

Finally, tables 6 and 7 present system parameter estimates for the ABL scenario. In this case a 1 m telescope and sub-apertures of 0.3 m in diameter with 0.3 m separation were considered. The propagation ranges were 100 km and 300 km. The estimates in Tables 5-7 also show that the image motion can be accurately measured.

TABLE 1. PROOF-OF-CONCEPT TEST

$$L = 300M, \lambda = 0.63 \times 10^{-6}M, 2a_0 = 0.09M, d = 0.11M, \mu = 0.11M$$

Structure Parameter	$c_n^2, M^{-2/3}$	10^{-14}	5×10^{-14}	10^{-13}	5×10^{-13}
Coherence Parameter	r_0, cm	5.5	2.1	1.4	0.56
Long-Exposure Beam Size	$\varphi_{\text{eff}}, \mu\text{Rad}$	5	12	17.6	46.6
RMS Beam Wander	$\sigma_c, \mu\text{Rad}$	3.6	8	11.4	25.6
Short-Exposure Beam Size	$\varphi_{\text{ST}}, \mu\text{Rad}$	3.5	4.5	13.4	39
RMS Differential Motion	$\sigma_d, \mu\text{Rad}$	2.9	6.5	9.1	20.4

TABLE 2. AIRBORNE LASER ADVANCED CONCEPTS TESTBED

Focused beam ($\frac{L}{F_i} = 1$) , $\lambda = 0.532 \times 10^{-6} \text{M}$, $2a_0 = 0.2 \text{M}$, $d = 0.16 \text{M}$, $\mu = 0.16 \text{M}$, $C_n^2 = 2 \times 10^{-17} \text{M}^{-2/3}$

Range	L, km	10	20	30	40	50
Coherence Parameter	r ₀ ,cm	22	15	12	9.9	8.6
Long-Exposure Beam Size	φ _{eff} ,μRad	1.2	1.6	1.9	2.6	2.4
RMS Beam Wander	σ _c ,μRad	0.8	1.1	1.4	1.6	1.8
Short-Exposure Beam Size	φ _{ST} ,μRad	0.9	1.1	1.3	2.1	1.6
RMS Differential Motion	σ _d ,μRad	0.7	1.0	1.2	1.4	1.6

TABLE 3. AIRBORNE LASER ADVANCED CONCEPTS TESTBED

Focused beam ($\frac{L}{F_i} = 1$) , $\lambda = 0.532 \times 10^{-6} \text{M}$, $2a_0 = 0.2 \text{M}$, $d = 0.16 \text{M}$, $\mu = 0.16 \text{M}$, $C_n^2 = 6 \times 10^{-17} \text{M}^{-2/3}$

Range	L, km	10	20	30	40	50
Coherence Parameter	r ₀ ,cm	12	7.7	6	5.1	4.4
Long-Exposure Beam Size	φ _{eff} ,μRad	1.9	2.7	3.3	3.9	4.5
RMS Beam Wander	σ _c ,μRad	1.4	2.0	2.4	2.8	3.2
Short-Exposure Beam Size	φ _{ST} ,μRad	1.25	1.8	2.3	2.8	3.2
RMS Differential Motion	σ _d ,μRad	1.21	1.7	2.1	2.4	2.7

TABLE 4. AIRBORNE LASER ADVANCED CONCEPTS TESTBED

Focused beam ($\frac{L}{F_i} = 1$), $\lambda = 0.532 \times 10^{-6} \text{M}$, $2a_0 = 0.2 \text{M}$, $d = 0.16 \text{M}$, $\mu = 0.16 \text{M}$, $C_n^2 = 2 \times 10^{-16} \text{M}^{-2/3}$

Range	L, km	10	20	30	40	50
Coherence Parameter	r_0, cm	5.7	3.7	3.0	2.5	2.2
Long-Exposure Beam Size	$\varphi_{\text{eff}}, \mu\text{Rad}$	3.5	5.3	6.7	7.6	9.1
RMS Beam Wander	$\sigma_c, \mu\text{Rad}$	2.6	3.6	4.4	5.1	5.7
Short-Exposure Beam Size	$\varphi_{\text{ST}}, \mu\text{Rad}$	2.5	3.9	5.0	5.7	7.1
RMS Differential Motion	$\sigma_d, \mu\text{Rad}$	2.2	3.1	3.8	4.4	5.0

TABLE 5. ASTRONOMY

$L = 20 \text{km}$, $\lambda = 0.351 \times 10^{-6} \text{M}$, $2a_0 = 0.5 \text{M}$, $\varepsilon = 90^\circ$, $d = 0.16 \text{M}$, $\mu = 0.16 \text{M}$

Structure Parameter	$\overline{C_n^2}, \text{M}^{1/3}$	2.2×10^{-13}	7×10^{-13}	2.2×10^{-12}	10^{-11}
Coherence Parameter	r_0, cm	13.1	6.5	3.3	1.3
Long-Exposure Beam Size	$\varphi_{\text{eff}}, \mu\text{Rad}$	1.0	2.1	4.1	10.1
RMS Beam Wander	$\sigma_c, \mu\text{Rad}$	0.8	1.4	2.4	5.2
Short-Exposure Beam Size	$\varphi_{\text{ST}}, \mu\text{Rad}$	0.7	1.6	3.3	8.7
RMS Differential Motion	$\sigma_d, \mu\text{Rad}$	0.7	1.3	2.3	5.0

TABLE 6. AIRBORNE LASER SCENARIO

$$L = 100\text{km}, \lambda = 1.06 \times 10^{-6}\text{M}, 2a_0 = 1\text{M}, d = 0.3\text{M}, \mu = 0.3\text{M}$$

Structure Parameter	$c_n^2, \text{M}^{-2/3}$	10^{-18}	5×10^{-18}	10^{-17}	5×10^{-17}
Coherence Parameter	r_o, cm	79.1	30.2	20.0	7.6
Long-Exposure Beam Size	$\phi_{\text{eff}}, \mu\text{Rad}$	0.6	1.4	2.1	5.4
RMS Beam Wander	$\sigma_c, \mu\text{Rad}$	0.46	1.0	1.45	3.25
Short-Exposure Beam Size	$\phi_{\text{ST}}, \mu\text{Rad}$	0.4	0.95	1.5	4.3
RMS Differential Motion	$\sigma_d, \mu\text{Rad}$	0.4	0.92	1.3	2.9

TABLE 7. AIRBORNE LASER SCENARIO

$$L = 300\text{km}, \lambda = 1.06 \times 10^{-6}\text{M}, 2a_0 = 1\text{M}, d = 0.3\text{M}, \mu = 0.3\text{M}$$

Structure Parameter	$c_n^2, \text{M}^{-2/3}$	10^{-18}	5×10^{-18}	10^{-17}	5×10^{-17}
Coherence Parameter	r_o, cm	41.0	15.6	10.3	3.9
Long-Exposure Beam Size	$\phi_{\text{eff}}, \mu\text{Rad}$	1.0	2.6	3.4	10.0
RMS Beam Wander	$\sigma_c, \mu\text{Rad}$	0.8	1.8	2.5	5.6
Short-Exposure Beam Size	$\phi_{\text{ST}}, \mu\text{Rad}$	0.7	1.9	2.3	8.3
RMS Differential Motion	$\sigma_d, \mu\text{Rad}$	0.7	1.6	2.2	5.0

3.2.2 Lidar calculations

The uncertainty in the measurement of an image centroid position due to photon statistics is given by

$$S_x^2 = \frac{\sigma_x^2}{N_L} \left(1 + \frac{N_s}{N_L} \right) \quad (10)$$

where S_x is the position uncertainty, σ_x is the image width, N_L is the number of laser photons in the image, and N_s is the number of sky background photons in the image. The number of laser photons was calculated by using the lidar equation, which can be expressed as

$$N = N_o \left(\frac{A}{R^2} \right) k \left(\frac{c\tau}{2} \right) \beta \exp \left[-2 \int_o^R \sigma(r) dr \right], \quad (11)$$

where N is the number of photons received,

N_o is the number of photons transmitted in each laser pulse,

A is the receiver area (m^2), R is the range (m),

k is the optical efficiency (dimensionless),

c is the speed of light ($3 \times 10^8 m/s$),

τ is the sampling interval (s),

β is the backscatter coefficient ($m^{-1}sr^{-1}$), and

$\sigma(r)$ is the atmospheric extinction coefficient (m^{-1}).

The number of photons transmitted is related to the energy per pulse E in Joules by

$$N_o = \lambda E / hc, \quad (12)$$

where λ is the wavelength (in meters), h is Planck's constant, $6.63 \times 10^{-34} Js$, and c is the speed of light.

The number of sky background photons was calculated from the equation

$$P = LA\Omega B, \quad (13)$$

where P is the received power (W),

L is the spectral radiance of the sky ($W/m^2 - sr - micron$),

A is the receiver area (m^2),

Ω is the receiver solid angle (sr), and

B is the receiver's optical bandpass ($microns$).

The solid angle $\Omega(sr)$ can be calculated from field of view angle $\phi(rad)$ by using the relation

$$\Omega = \frac{\pi}{4} \phi^2 \quad (14)$$

The number of sky background photons that will be received by the LIDAR during the sampling interval τ is given by

$$N_s = P \tau \lambda / hc, \quad (15)$$

so by substituting the expression in Eq. (13) for P we find

$$N_s = LA\Omega B \tau \lambda / hc. \quad (16)$$

In order to estimate centroid position uncertainties, the numbers of photons N_L and N_s were calculated by using Eqs. (11) and (16), respectively, and these numbers were then used in Eq. (10). In each case, the image width σ_x was taken to be the short-exposure beam size value listed in Tables 1 - 7, and the image field of view angle ϕ was also taken to be the short-exposure beam size.

For each scenario, the optimum laser wavelength was chosen and then the input parameters for the lidar equation were chosen based on specifications of commercial laser, choices of receiver and operational parameters, and modeled or published values of atmospheric characteristics. The results of these calculations are shown in Tables 8 - 11.

Table 8. ABL-ACT – 50 km Range

C_n^2	RMS Position Error (μrad)		RMS Diff. Motion (μrad)
	(day)	(night)	
1E-17	2.33E-02	2.33E-02	1.1
1E-16	8.47E-02	8.46E-02	3.5
1E-15	4.23E-01	4.15E-01	11

Table 9. ASTRONOMY

C_n^2	RMS Position Error (μrad)		RMS Diff. Motion (μrad)
	(night)		
2.20E-13	4.09E-03		0.7
7.00E-13	9.35E-03		1.3
2.20E-12	1.93E-02		2.3
1E-11	0.05		5

Table 10. ABL – 100 km Range

C_n^2	RMS Position Error (μrad)		RMS Diff. Motion (μrad)
	(day)	(night)	
1.00E-18	5.54E-03	5.54E-03	0.4
5.00E-18	1.32E-02	1.32E-02	0.92
1.00E-17	2.08E-02	2.08E-02	1.3
5E-17	0.06	0.06	2.9

Table 11. ABL – 300 km Range

C_n^2	RMS Position Error (μrad)		RMS Diff. Motion (μrad)
	(day)	(night)	
1.00E-17	1.67E-02	1.67E-02	0.7
1.00E-16	4.57E-02	4.53E-02	1.6
1.00E-15	5.49E-02	5.49E-02	2.2
5.00E-15	0.22	0.20	5

In Tables 8 - 11, the RMS position errors are at most a few percent of the expected differential motions due to turbulence, during either day or night. This means that the position errors due to photon statistics will have a small effect on the measurements of C_n^2 . The conclusion of the performance analysis is therefore that the proposed DIM lidar technique is practical in several scenarios, including the ABL Advanced Concepts Testbed, astronomy, and as a Tactical Decision Aid (TDA) for the ABL aircraft.

3.3 Hardware and Software Development

3.3.1 3.3.1 Hardware development

The purpose of the field experiment was to validate the DIM lidar concept by measuring the strength of atmospheric turbulence with this method and with an independent sensor. The specific objectives were two-fold: 1) to show that the method accurately measures C_n^2 values throughout a range of turbulent conditions, and 2) to show that the two-way (lidar) technique gives the same results as the conventional, one-way DIM method.

To simplify the instrumentation, we built a hard-target analog of a DIM lidar. A diagram of this apparatus is shown in Fig.3. The beam from a 25 mW He-Ne laser was expanded with a high-quality optical system 10 cm in diameter and focused on a diffuse target. The

receiver system was based on a 40-cm diameter Newtonian telescope. An aperture mask with two 10 cm diameter sub-apertures separated by 30 cm was mounted in front of the telescope to select portions of the incoming wavefront. Two small glass plates were used to displace the images in the image plane.

A lens assembly behind the focal plane formed a magnified image in a CCD camera and allowed the differential motion to be measured accurately. An interference filter between the lenses rejected all but a narrow range of wavelengths centered on the laser line and improved the signal-to-noise ratio by blocking sunlight. The CCD had a 650 x 693 pixel array and a digital interface with a Pentium-based computer through the PCI bus. A sampling rate of 100 Hz was achieved by reading a 128 x 64 pixel sub-array that covered both images. Software was developed to calculate the centroid position for each image, to compute the variance σ_d^2 , and finally to calculate C_n^2 . For each data point, 1000 data frames were acquired to estimate the DIM variance.

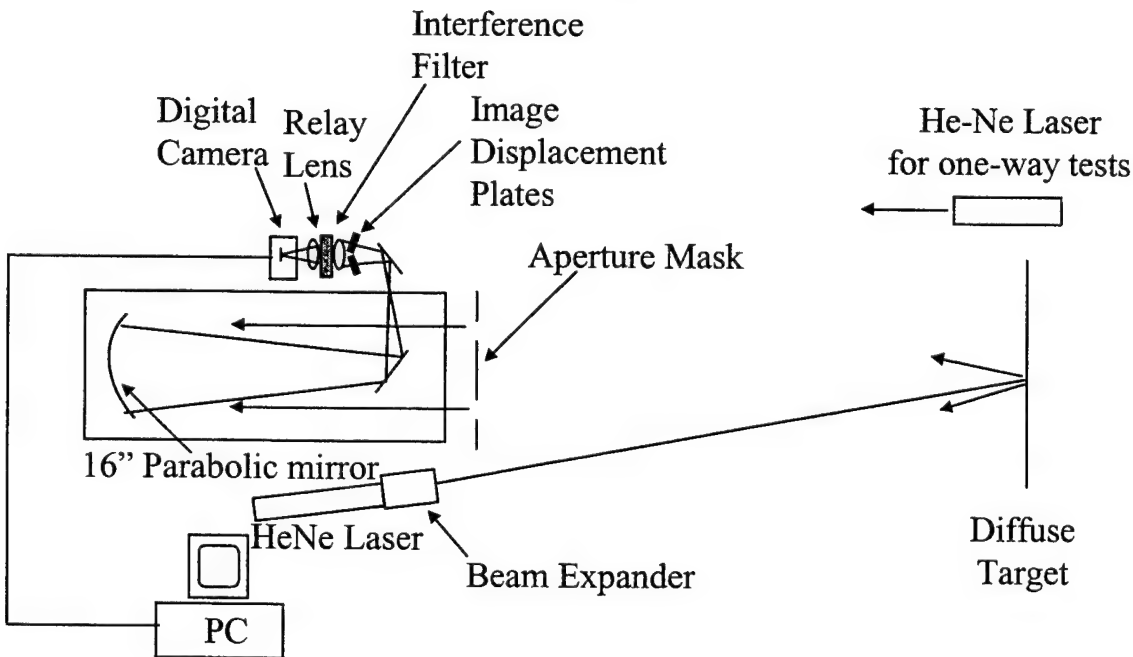


Fig. 3. Diagram of the hard-target analog of the DIM lidar used in the field test.

3.3.2 Software development

The purpose of the specially developed software was to acquire data and compute the structure characteristic C_n^2 . The software package included the data acquisition software, the algorithm for determining the energy centroid, the algorithm for calculating rms differential motion, σ_d , and the algorithm for C_n^2 .

The frame rate was a primary concern in the data acquisition software development. The camera was shipped with a simple software development kit (SDK) and C example programs. The full focal plane array of the EDC 2000N camera consisted of 650x693 pixels. A pixel read time of about 2 million pixels/sec limited the frame rate to about 12 frames/sec. In order to read frames at rates of 80 Hz –100Hz, which were necessary for the planned experiment, the sub-array option was employed. The sub-array size was computed to encompass the expected separation of the spots in the image plane as well as the expected size of the spots and their movement as presented in Table 1.

Based on the estimates of spot separations, spot size and spot motion characteristics, a 128x64 pixel sub-array was selected. The read-out time for this sub-array was about 4 ms. A variable integration time was selected, in the range from 1 ms to 6 ms, to accommodate variations of the laser irradiance and a background. Full frame read-out time includes an integration time, a mean overhead time (which ranges from 2-3 ms per frame), and the pixel transfer time. Depending on the integration time, a frame rate in the range from 80 frames/sec to 120 frames/sec was demonstrated with the sub-array option.

The software operates as follows: first, the imager is blocked and a background of the full focal plane array is recorded. Then, the software captures a number of frames, subtracts the background from the frames, and computes the mean X and Y values of the centroids for all of the frames. The mean centroid location is used as the center of the analysis region. The SDK requires that the sub-region be attached to the left side of the entire array. The software can place the analysis region anywhere in the image inside the focal

plane array. However, the performance degrades as the analysis region moves away from the left side of the image because the camera is transferring additional pixels.

Once the alignment of the analysis region is completed, the software collects a set of 1000 data frames, transfers them to memory, and subtracts the background from each frame. The X and Y centroids are then computed for all of the frames. The centroid is computed as $X = \sum_i p_i \times l_i / \sum_i p_i$, where p_i is the image brightness at the i^{th} pixel, and l_i is the distance from the pixel to the center of the sub-array. From the centroids the differences are computed: $\alpha(j) = X_r - X_l$ and $\beta(j) = Y_r - Y_l$, where j is the number of the frame. Once all the differences have been computed, the software computes the mean and variance of the differential image motion and the structure characteristic C_n^2 from Eq. (4).

3.4 Field test

In order to show that the DIM lidar technique gives correct values of C_n^2 , we tested the hard-target analog against a conventional scintillometer manufactured by Scientific Technology, Inc, which measures scintillations of an infrared light and provides path-averaged readings of C_n^2 . The test was performed on a 300 *m* horizontal path in an open area covered with a grass. The instrumentation included the hard-target analog of the DIM lidar, the scintillometer, and weather instruments. Weather instruments included a wet and dry bulb hygrometer, an ultrasonic anemometer, and an infrared temperature sensor. The hygrometer provided air temperature and relative humidity, the anemometer measured wind velocity and direction, and the infrared sensor provided the ground temperature. To show that the DIM variances on two-way and one-way paths coincide with each other, we also collected data by using a conventional one-way DIM

configuration. In this case, a laser source at the diffuse target location was used to illuminate the DIM receiver.

The DIM sensor and the scintillometer were operated on adjacent paths. The diffuse target and the scintillometer transmitter were located at one end of the measurement path, and the DIM sensor, the scintillometer receiver, and the data acquisition system were located at the other end of the path. The anemometer was placed in the middle range. The data from both optical instruments were collected at 10-second intervals. The height of the optical path above the terrain was 1.4 m at both ends and it varied from 0.75 m to 2.3 m at various points along the path. The average height was 1.4 m.

The field experiment was performed on October 5 – 7, 1999. On October 7, the data were continuously collected from 0845 to 1245 EDT. The sky was clear initially, with some cumulus clouds toward the end of the test. The air temperature increased from 15 to 22 $^{\circ}\text{C}$, and the grass was dew-covered for most of the test. The wind was calm at first, changing to a light breeze (<5 m/s).

3.5 Analysis of the data

The data collected in the test were processed and analyzed by using the specially developed software. Figure 4 shows a time history of the October 7 measurements. The C_n^2 values were measured with the DIM sensor in both two-way and one-way configurations, and also with the scintillometer. The results are plotted as two-minute averages for clarity. Figure 4 shows that the C_n^2 values measured with the hard-target analog of the DIM lidar and with the scintillometer agree well with each other. It also shows that the data collected with the one-way and two-way DIM configurations are consistent with each other and that they both agree with the scintillometer data.

A scatter plot of the 10 second data collected with the hard-target analog and the scintillometer is shown in Figure 5. This also shows good agreement between the

readings from the two sensors. The slope of the straight line obtained from a linear regression analysis is 1.2 and the regression coefficient is 0.77. The differences between the readings from the DIM sensor and scintillometer could be partly due to variations of C_n^2 along the path. The path-weighting function for the DIM sensor is maximal near the DIM receiver. At this point, the height above the ground is 1.4 m. The path-weighting function for the scintillometer is maximal at the middle range, where the height is about 2.3 m. The well-known¹¹ decrease of C_n^2 with height would be expected to lead to a difference between the readings from the two sensors. Different local albedos and amounts of surface moisture at the near end of the path and at the middle range could also contribute to the observed differences between the C_n^2 values.

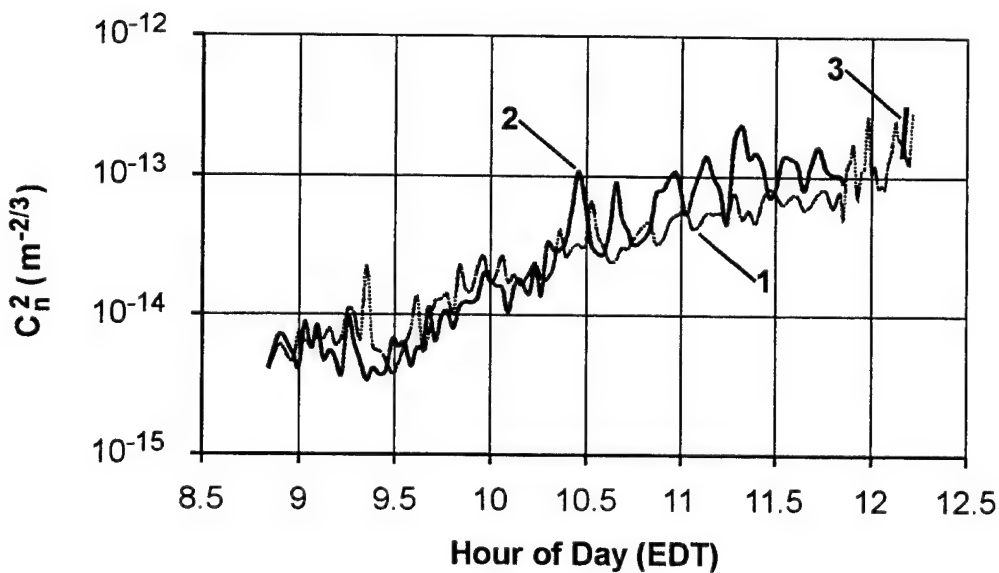


Fig. 4. Time histories of the values measured with a commercial scintillometer and the hard-target analog of the DIM lidar. Curve 1: scintillometer, Curve 2: hard-target analog, Curve 3: one-way configuration of the DIM sensor.

The measurements reported here were performed throughout a range of turbulence conditions. The strength of turbulence is usually characterized by the Rytov variance, $\sigma_I^2 = 1.23k^{7/6}C_n^2L^{11/6}$. For the wavelength of $\lambda = 0.63 \cdot 10^{-6} m$, distance

$L = 300m$, and $C_n^2 \leq 3 \cdot 10^{-13} m^{-23}$ the Rytov variance was $\sigma_I^2 \leq 2$, so the validation test was performed in the regime of weak and intermediate scintillation.

The experimental results validate the concept of the DIM lidar and show that the structure characteristic C_n^2 can be measured accurately with this technique. The theoretical and experimental underpinnings are now in place to develop a true DIM lidar that will employ a pulsed laser, atmospheric backscatter, and a range-gated receiver to measure profiles of C_n^2 .

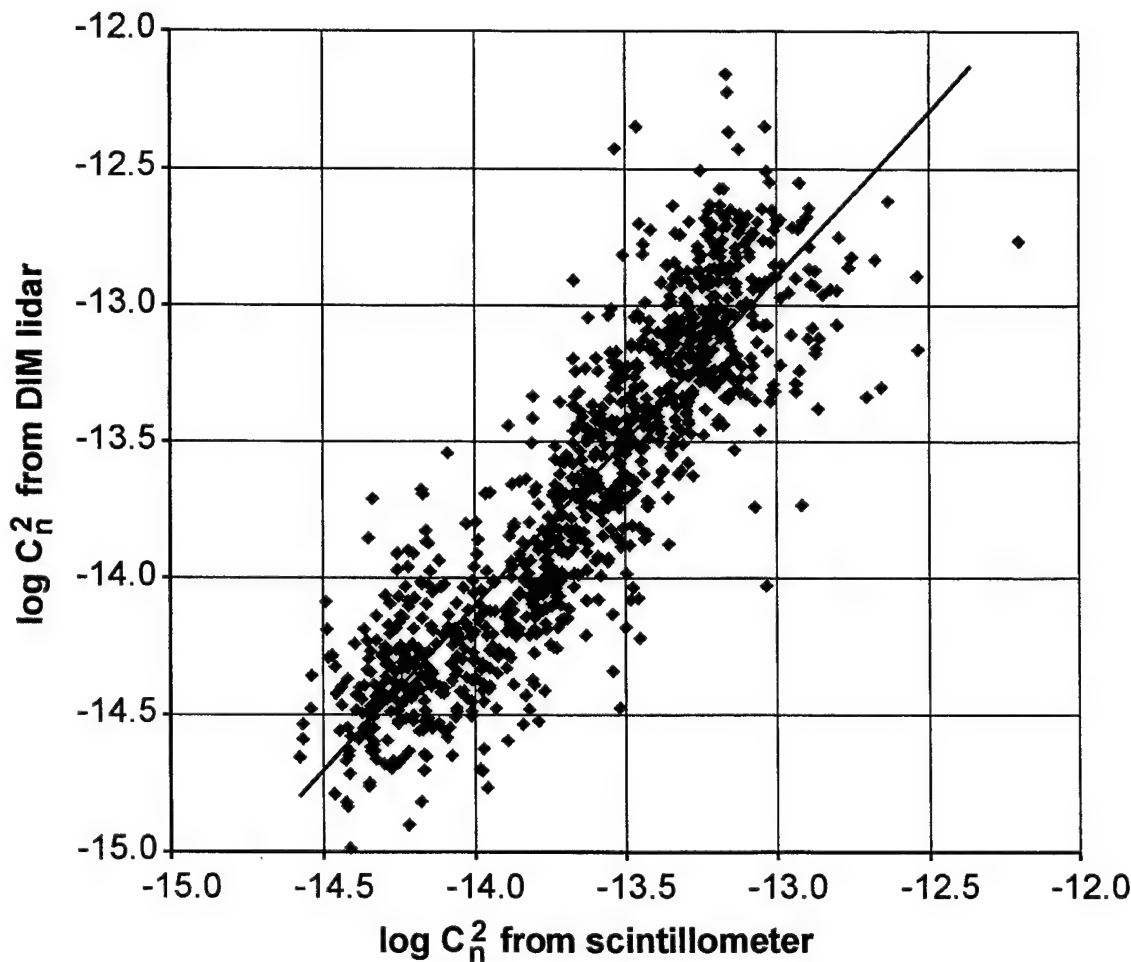


Fig. 5. Scatter plot of the measurements with the hard-target analog of the DIM lidar versus the scintillometer data.

3.6 Scientific paper

A scientific paper was written and submitted to Optics Letters. The paper was accepted for publication.

3.7 Effects of laser speckles and scintillations

Air Force Experience with an astronomical Differential Image Motion Monitor (DIMM) at the Starfire Optical Range (SOR)²³ and at North Oscura Peak (NOP)²³ has shown that a speckle phenomenon degrades the performance of the sensor during conditions of strong turbulence. The primary purpose of the analysis presented in this section, which was documented in a Technical Memorandum and sent to the sponsor, was to assess the effect of this phenomenon on the performance of our proposed DIM lidar.

3.7.1 Laser speckle phenomenon

It is known that for some turbulent conditions a star image breaks into multiple speckles. This phenomenon occurs^{12,13} when the telescope diameter, D , exceeds the Fried parameter, r_0 , $D/r_0 > 1$. The speckles can introduce a measurement error in the centroid position for both open-loop tilt measurements for astronomical observations and for sensing of r_0 with a DIM sensor. A simulation performed by a researcher at SOR revealed that the maximum error in the centroid position is introduced when the number of speckles in the image plane, $N \approx (D/r_0)^2$, is severely limited, or $D/r_0 \approx 1 - 3$. The error decreases with an increasing number of speckles, N , because multiple speckles compensate each other. According to the simulation performed by Capt. J. Barchers, the speckle-induced relative error in the centroid position for $D/r_0 \approx 1 - 3$ is in the range of 15-20 %. However, this estimate is not applicable to the DIM lidar because the phenomenon observed at SOR and NOP²³ only occurs with point sources such as a star or a distant laser and does not occur with the DIM lidar since the scattering volume illuminated by a laser beam is not a point source.

3.7.2 Coherent point source

In the conventional DIM technique, a receiver is illuminated by a coherent point source (a star or a laser). If the initial radius of the beam, a_0 , satisfies the condition $\Omega = ka_0^2 / L \ll 1$, then the source is a point source. Here $k = 2\pi / \lambda$ is the wavenumber and L is the measurement range. The spatial coherence of an optical wave is degraded exclusively by turbulence. For a plane wave the mutual coherence function is expressed through the corresponding phase structure function, D_s ,

$$\Gamma_2^{(t)} = \exp\left(-\frac{1}{2}D_s(\rho)\right) = \exp\left(-\left(\rho / \rho_0\right)^{5/3}\right), \quad (17)$$

where ρ_0 is the coherence radius, $\rho_0 = (1.45k^2 LC_n^2)^{-3/5}$, and C_n^2 is the refractive index structure characteristic. This scale relates to the Fried parameter by $r_0 = 2.1\rho_0$. For a spherical wave, or point source, the coherence radius equals

$$\rho_C = (1.45k^2 \int_0^L C_n^2(z) (1 - z/L)^{5/3} dz)^{-3/5}, \quad (18)$$

and $\rho_C = 1.8\rho_0$ for $C_n^2 = \text{const}$.

In the case of a DIM lidar, a transmitted beam illuminates a scattering volume which contains a large number of small particles, or molecules, randomly distributed throughout the volume. The separation of the particles is generally much greater than an optical wavelength. As a consequence, the scattered radiation from one scatterer will be completely incoherent with respect to that from any other.^{14,15} This mechanism is identical to that for a diffuse target, or extended incoherent source. The longitudinal size of the scattering volume is determined by the range gate of the imager, which varies from several hundreds of meters to several kilometers. The transverse size of the volume coincides with the short-exposure size of the beam, and typical values of the Fresnel parameter for the scattering volume size are typically greater than unity, $\Omega > 1$.

Due to random phase perturbations at different positions of the scatterers under the reflection of the coherent light from the multiple scatterers a speckle pattern in the image plane occurs,^{12,14} but this is a different phenomenon from the stellar image case, and the speckle scales are much smaller. This is shown in the next section

3.7.3 Extended incoherent source

References 16 and 17 give the mutual coherence function of the light scattered by multiple scatterers in the turbulent atmosphere as

$$\Gamma_{(2)}(L, \bar{R}, \bar{\rho}) = \Gamma_{(2)}^{(a)}(L, \bar{R}, \bar{\rho}) \times \Gamma_{(2)}^{(t)}(L, \bar{R}, \bar{\rho}), \quad (19)$$

where $\Gamma_{(2)}^{(a)}$ is the mutual coherence function of a laser beam scattered in a homogenous medium ($C_n^2 = 0$), and $\Gamma_{(2)}^{(t)}$ is the coherence function of a spherical wave in a turbulent atmosphere. The function $\Gamma_{(2)}^{(a)}$ has the form

$$\Gamma_{(2)}^{(a)} = \frac{\beta a_{\text{eff}} I_0}{L^2} \exp\left[-\frac{\rho^2}{\rho_{ca}^2} + \frac{ik}{L} \bar{R} \bar{\rho}\right], \quad (20)$$

where $\rho_{ca} = L / ka_{\text{eff}}$ is the coherence radius determined by the van Cittert-Zernike theorem,¹⁸ a_{eff} is the effective radius of the transmitted beam, β is the backscatter coefficient, and I_0 is the laser intensity. In most cases the coherence radius, ρ_{ca} , is much smaller than the turbulent coherence scale, $\rho_{ca} \ll \rho_c$. As a consequence, the first term in equation (12) is predominant, and the coherence scale of the scattered light equals ρ_{ca} . Consequently, the size of the image, which is determined by diffraction of the coherence scale, ρ_{ca} , $a_i = f / k \rho_{ca}$, where f is the focal length, coincides with the angular size of the transmitted beam, $\varphi_{\text{eff}} = a_i / f = a_{\text{eff}} / L$. Thus, the size of the image is determined by the angular size of the beam φ_{eff} , not by turbulence as for a point source.

Now we estimate the number of speckles in the image spot of a DIM lidar for various scenarios. In the proof-of concept test in Phase I, a CW laser with $\lambda = 0.63 \mu m$ was used. The initial diameter of the Gaussian beam was $2a_0 = 6.4 cm$, and the receiver diameter was $2a_R = 10 cm$. The diffractive size of the beam focused at a distant diffuse target, $\varphi_d = 1/ka_0$, is $\varphi_d = 3.1 \mu rad$. However, due to a multi-mode structure of the laser, the actual beam size was about $\varphi_{eff} = 4 \times \varphi_d$. Since for the aperture of $2a_R = 10 cm$ the speckle size, $\varphi_s = 1/ka_R$, is $\varphi_s = 1.8 \mu m$, the number of speckles in the reflected spot is $N = (\varphi_{eff}/\varphi_s)^2 = 48$. The number of speckles, N , increases with the strength of turbulence because turbulent broadening of the beam increases φ_{eff} .

Figures 6 a-c show images collected in preliminary tests of the hard-target analog of a DIM lidar. The images were collected in the hallway over a 50 m path without a heater (6 a), this case corresponds to very weak turbulent conditions, over a 50 m path with a heater (6 c), this case corresponds to very strong turbulence, and over 150 m outdoors during daytime (6 b). The last case corresponds to moderate turbulent conditions. It is seen that for all conditions the number of speckles is large, $N >> 1$, therefore the error in the centroid position caused by speckles is expected to be small. Numerical simulation of a single shot image for a coherent lidar (see Ref. 8, Fig 2) provides a speckle pattern which is similar to those shown in Figures 6 a and b.

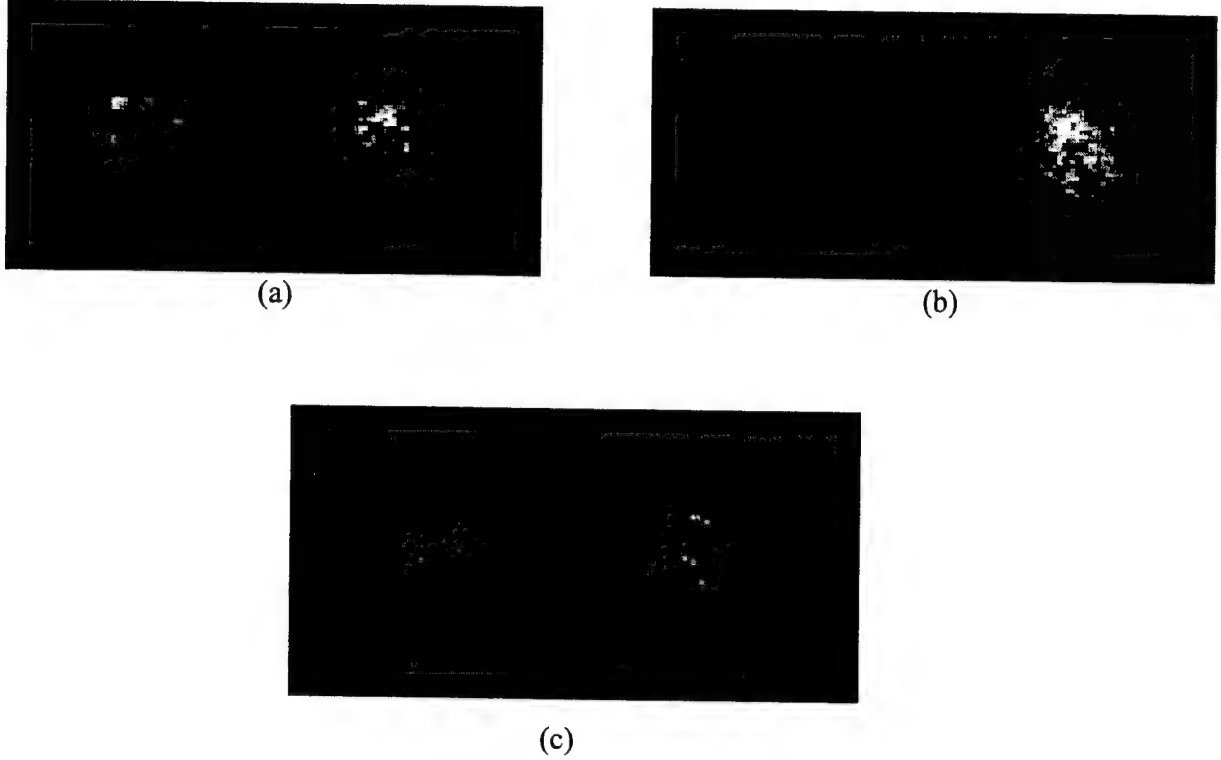


Figure 6 a-c. Images collected with a hard-target analog of the DIM lidar in very weak (a), moderate (b), and very strong turbulence condition (c).

Considering an eye safe uv lidar, the maximum measurement range at the horizontal path at NOP is limited by the transmittance of the UV light to about $L = 20$ km. For $L = 20$ km and a maximum value of $C_n^2 = 2.7 \cdot 10^{-16} m^{-2/3}$, the short-exposure beam size at NOP is $\varphi_{eff} \approx 7.6 \mu rad$, therefore the number of speckles is $N=118$ for $2a_R= 16 cm$, and it is $N=236$ for $2a_R= 32 cm$. For the astronomical scenario with a maximum range of $L= 20$ km and zenith angle of 45° , $N= 95$ for $2a_R= 16 cm$, and $N=190$ for $2a_R = 32 cm$.

The long-exposure beam radius was estimated from Eq.(7), the estimates for the short-exposure size of the beam were obtained from Eq.(8), and the one-axis beam wander variance was computed from Eq. (9). From equation (7) it is seen that, for long paths and strong turbulence, when the contribution of the turbulent term is predominant, $\varphi_{eff} \approx (C_n^2)^{3/5}$, the number of speckles in the reflected spot increases with the strength of

turbulence as $N \approx (C_n^2)^{6/5}$ thus reducing the speckle-induced error for the centroid. In the next section we will quantify this effect

3.7.4 Error analysis

To quantify the measurement error in the centroid position caused by laser speckles, the centroid variance in a speckle image is calculated in the absence of turbulence. A centroid is given by $C = P^{-1} \iint_{\Sigma} R I(R) d^2 R$, where P is the flux through the aperture, $I(R)$

is the intensity distribution in the image plane, and $\Sigma = \pi a_R^2$ is the area of the receiving aperture. By using this expression, the centroid variance σ_{α}^2 can be expressed through the intensity covariance given by

$$\sigma_{\alpha}^2 = P^{-2} \iint d^2 R d^2 \rho A(R) A(\rho) (R^2 - \rho^2 / 4) \langle I(\vec{R} + \vec{\rho} / 2) I(\vec{R} - \vec{\rho} / 2) \rangle. \quad (21)$$

Here $A(R)$ is the aperture function of the receiver, and the angular brackets denote ensemble averaging.

Due to random phase perturbations of the scattered light, the optical field from a scattering volume or a diffuse target, is a complex Gaussian random variable.^{12,14,15} The fourth moment of the random Gaussian variable relates to the second moment by the equation,²⁰

$$\langle I_1 I_2 \rangle = |\Gamma_2|^2 + \langle I \rangle^2, \quad (22)$$

where Γ_2 is given by equation (12). By using equations (19) and (22), as well as a Gaussian approximation for the aperture transmission function ($A(R) = \exp(-R^2 / a_R^2)$), one can obtain $\sigma_{\alpha}^2 = \rho_I^2$, where ρ_I is the intensity correlation scale. From equation (22) it follows that the intensity correlation scale is given by $\rho_I = \rho_{c,a} / \sqrt{2}$.

Since the structure characteristic, C_n^2 , is expressed through the mean square difference $\langle(\alpha_1 - \alpha_2)^2\rangle$, where α_1 and α_2 are the centroids of the two images, the absolute error for C_n^2 caused by the speckle phenomenon equals double the error for the centroid, or $\Delta C_n^2 = 2\sigma_\alpha^2$. We estimate the relative error, $\varepsilon = \Delta C_n^2 / C_n^2$, for the case $L \geq 10\text{km}$, when the effective size of the beam is determined by the turbulence, or the third term in equation (7). The estimates show that the rms differential motion, σ_{DM} , in this regime relates to the short-exposure beam radius by $\sigma_{DM} = \varphi_{eff} / \gamma$, where γ is in the range from 1 to 1.7. Since $C_n^2 \approx \sigma_{DM}^2$, the relative error, $\varepsilon = \Delta C_n^2 / C_n^2$, equals

$$\varepsilon = 2\sigma_\alpha^2 / \sigma_{DM}^2 = \gamma^2 / N. \quad (23)$$

As the number of speckles for $2aR = 16\text{ cm}$ is $N=118$, the relative error for C_n^2 is $\varepsilon \leq 3\%$. For the receiver with $2aR = 32\text{ cm}$ the number of speckles is $N=236$, and the relative error is $\varepsilon \leq 1.5\%$. The implication is that, due to the large number of speckles in the reflected spot, the measurement error for the centroid position and consequently for C_n^2 measured with the DIM lidar is small.

3.7.5 Laser scintillations

It is well known that the planets twinkle weaker than stars situated at the same zenith angle.¹¹ Tatarskii¹¹ studied this phenomenon theoretically and showed that if the angular size of the incoherent source exceeds the angular size of the Fresnel zone, $\varphi_R \geq \sqrt{\lambda/L}$, then the scintillations are averaged over the size of the source. According to Tatarskii's estimates,¹¹ the scintillation variance reduces by a factor of about 3 when $\varphi_R / \sqrt{\lambda/L} \geq 1$.

Researchers from NOAA used the same phenomenon to develop a saturation-resistant optical scintillometer.²¹ In this scintillometer, both the incoherent source and the receiver

exceed the radius of a Fresnel zone for the optical path, $\sqrt{\lambda L}$. It was shown that, for such a source and receiver, there is no saturation effect even in the strong turbulence regime, and the calibration remained unchanged in both the weak and strong scintillation regime. Experimental validation performed over an $L=500\text{m}$ path in strong turbulence, when the Rytov variance, $\beta_0^2 = 1.23k^{7/6}L^{11/6}C_n^2$, $\beta_0^2 = 25$, confirmed this conclusion.

As the size of the scattering volume and the receiver in the DIM lidar exceeds the Fresnel zone, a similar saturation resistance capability is expected. Indeed, for the moderate strength of turbulence at NOP, $C_n^2 = 6 \cdot 10^{-17} \text{ m}^{-2/3}$, which corresponds to $r_0 = 10\text{cm}$ at $\lambda = 1.06\mu\text{m}$, the Rytov variance is $\beta_0^2 = 1.6$. However, the effective size of the beam for $\lambda = 0.351\mu\text{m}$ and $L = 20 \text{ km}$ exceeds the angular size of the Fresnel zone, $\sqrt{\lambda/L} = 4\mu\text{rad}$, and the receiver with an aperture diameter of $2a_R = 32 \text{ cm}$ is twice as large as the Fresnel zone. For this reason one can expect that, due to averaging of intensity fluctuations over the scattering volume and the receiver, the scintillations will be reduced to the level of weak turbulence.

For the maximum strength of turbulence at NOP, $C_n^2 = 2.7 \cdot 10^{-16} \text{ m}^{-2/3}$, which corresponds to $r_0 = 4\text{cm}$ at $\lambda = 1.06\mu\text{m}$, the Rytov variance over an $L = 20 \text{ km}$ path is $\beta_0^2 = 7$. However, the effective size of the beam, φ_{eff} , increases with the strength of turbulence. As a consequence, for these conditions, the size of the beam is $\varphi_{\text{eff}} \approx 7.6\mu\text{rad}$, and it exceeds the Fresnel zone by a factor of 2. Due to averaging of the scintillations over the size of the scattering volume and the receiver, according to the preliminary estimates, one can expect that no saturation effect will be observed. The implication is that a DIM lidar, similar to the NOAA scintillometer, would be expected to be saturation resistant.

These estimates also show that for inclined propagation paths for astronomical scenarios, the weak scintillation regime will be observed during either day or night even for the strongest turbulence near the ground, if the zenith angle of the measurement path is $\theta \leq 60^\circ$.

3.7.6 Sky background

The high sky background level is responsible in part for the failure of a conventional DIM sensor to measure r_0 during daytime at SOR. In the DIM lidar this difficulty can be overcome through the use of a narrow band filter centered at the laser wavelength. This will provide a high signal-to- noise ratio for both day and night operations.

3.7.7 Design consideration

Another possible reason for the failure of the conventional DIM sensor in the presence of strong turbulence is that the size of the spots in the image plane and their motion could exceed the FOV, and/or two images could overlap. An accurate design of the DIM lidar using the flow-down design approach will allow for an accommodation of the expected spot size and motion for all operational conditions and propagation scenarios. The proof-of-concept test with a hard-target analog of the DIM lidar confirmed that even for the strongest turbulence the images of two spots are within the FOV and do not overlap.

3.7.8 Summary

The analysis performed leads to the following conclusions:

1. The phenomenon observed at SOR and NOP, which causes the images to break up into individual speckles, only occurs with point sources such as a star or a distant laser. Because the scattering volume of the DIM lidar will be an extended source, this particular phenomenon will not occur, regardless of the strength of turbulence.
2. Using a laser as a source of light will, however, cause a different kind of speckle pattern to appear in the images, due to the scattering of coherent light by multiple scatterers. This is different from the point source phenomenon, and the scale of these speckles is much smaller. For the scenarios and system parameters of interest here, there will typically be on the order of 100 or more speckles in each image. This will cause a r.m.s. measurement error in the centroid positions on the order of 1 percent,

regardless of turbulence conditions. Examples of images from our field demonstration apparatus that show this small-scale speckle pattern are included in this report.

3. Strong turbulence will cause scintillations in the laser beam, and this could, in principle, make measurements difficult due to large fluctuations in signal levels, but the sizes of the scattering volume and receiver aperture for the DIM lidar will tend to average out such effects.
4. The DIM lidar will employ a narrow-band optical filter to eliminate most of the sky background and maintain a good signal-to-noise ratio during daytime operation. This is possible because the DIM lidar will use a laser as a source of illumination, and a laser is a narrow-band source. Thus, the use of a narrow-band optical filter will eliminate most of the sky background and provide a good signal-to-noise ratio during daytime operation.

4.0 CONCLUSIONS

All the tasks and milestones of Phase I were accomplished. The following results were obtained:

1. The conceptual design and performance analysis of the DIM lidar were performed and the theoretical underpinnings of the DIM lidar were developed. It was shown that the differential image motion of a lidar return for the propagation scenarios of interest can be accurately measured;
2. The hardware of the hard-target analog of the DIM lidar was designed and built, and the software was developed;
3. A proof-of-concept test was performed. The experimental results validate the DIM lidar concept and show that the structure characteristic can be accurately measured with this technique;

4. The effects of the laser speckles and scintillations on the performance of the DIM lidar were analyzed. It was shown that the error in the centroid position caused by the laser speckles does not exceed a few percent. The DIM lidar has a saturation resistant capability, which is due to averaging of the scintillations over the scattering volume and the receiving aperture. The use of a narrow-band filter will eliminate most of the sky background and provide a good signal-to-noise ratio during daytime operation;
5. A scientific paper was written and submitted for publication to *Optics Letters*.

REFERENCES

1. A. C. Slavin, A. L. Wells, R. Q. Fugate, P. L. Leatherman, and J. J. Drexler, "A comparison of three methods of measuring the atmospheric coherence length," Proc. SPIE, **3125**, 241-249 (1997).
2. M. S. Belen'kii and V. L. Mironov, "Laser method for determining the turbulent parameter C_n^2 on the basis of light scattering by atmospheric aerosol," *Radiophys. Quantum Electron.*, **24**, 206-210(1981).
3. M. S. Belen'kii, A. A. Makarov, V. L. Mironov, and V. V. Pokasov, "Lidar measurements of structure characteristic of atmospheric turbulence," *Izv. Atmos. Oceanic Phys.*, **20**, 328-331(1984).
4. P. Gatt, R. G. Frehlich, S. M. Hannon, "Coherent laser radar atmospheric turbulence sensor," Proc. SPIE, **3381**, 220-229(1998).
5. M. S. Belen'kii, "The effect of residual turbulent scintillation and remote sensing technique for simultaneous determination of turbulent and scattering parameters of the atmosphere," *J. Opt. Soc. Am., A* **11**, 1150-1158(1994).
6. M. S. Belen'kii and G. G. Gimmestad, "Monostatic image distortion lidar technique for measuring intensity of atmospheric turbulence," Proc. SPIE, **2222**, 621-627(1994).

7. F. D. Eaton, W. A. Peterson, J. R. Hines, J. J. Drexler, A. H. Walde, and D. B. Soules, "Comparison of two techniques for determining atmospheric seeing," Proc. SPIE, **926**, 319-334(1988).
8. M. S. Belen'kii , "Tilt angular correlation and tilt sensing techniques with a laser guide star," Proc. SPIE, 2956, 206-217(1996).
9. A. M. Prokhorov, F. V. Bunkin, K. S. Gochelashvily, and V. I. Shishov, "Laser irradiance in turbulent atmosphere," Proc. IEEE **63**, 790-809(1975).
10. R. L. Fante, "Electromagnetic beam propagation in turbulent media," Proc. IEEE **63**, 1669-1692(1975).
11. V. I. Tatarskii, Wave Propagation in a Turbulent Medium, McGraw-Hill, New York, 1961.
12. J. M. Goodman, Statistical Optics, Ch.2, John Wiley and Sons, New York, 1985.
13. D. L. Fried, "Optical resolution through a randomly inhomogeneous medium for very long and very short exposures," J. Opt. Soc., Am., **56**, 1372-1379 (1966).
14. J. C. Dainty, Ed., Laser Speckle and Related Phenomena, Springer, New York, 1975.
15. Y. H. Churnside and H. T. Yura, "Velocity measurement using laser speckle statistics," Appl. Opt., **20**, 3539-3541(1981).
16. S. F. Clifford and S. Wandzura, "Monostatic heterodyne lidar performance: the effect of turbulent atmosphere," Appl. Opt., **20**, 514-516(1981).
17. M. S. Belen'kii, "Effect of atmospheric turbulence on heterodyne lidar performance," Appl. Opt., **32**, 5368-5372(1993).
18. M. Born and E. Wolf, Principals of Optics, Pergamon, New York, 1975.
19. P.Gatt, R. G. Frehlich, S. M. Hannon, "Coherent laser radar atmospheric turbulence sensor," Proc. SPIE, 3381, 220-229(1998).

20. S. M. Rytov, Yu. A. Kravtsov, and V. I. Tatarskii, "Principles of statistical radiophysics," in Wave Propagation Through Random Media, Springer Berlin, 1989, vol. 4.
21. Ting-I Wang, G. R. Ochs, and S. F. Clifford, "A saturation-resistant optical scintillometer to measure C_n^2 ," *Appl. Opt.*, 68, 334-338(1978).
22. S. F. Clifford, G. R. Ochs, and R. S. Lawrence, "Saturation of optical scintillation by strong turbulence," *J. Opt. Soc. Am.*, 64, 148-154(1974).
23. Private Communication with personnel from Starfire Optical Range (SOR) and North Oscura Peak (NOP), 1999

DISTRIBUTION LIST

DTIC/OCP
8725 John J. Kingman Rd, Suite 0944
Ft Belvoir, VA 22060-6218 1 cy

AFSAA/SAMI
1570 Air Force Pentagon
Washington, DC 20330-1570 1 cy

AFRL/VSIL
Kirtland AFB, NM 87117-5776 2 cys

AFRL/VSIH
Kirtland AFB, NM 87117-5776 1 cy

Applied Technologies, Inc.
1120 Delaware Ave.
Longmont, CO 80501 1 cy

Official Record Copy
AFRL/DEBA/Frank D. Eaton 9 cys